Video-Rate Non-Raster AFM Imaging With Cycloid Trajectory

Nastaran Nikooienejad, Afshin Alipour, Mohammad Maroufi, and S. O. Reza Moheimani

***Abstract*— We demonstrate the application of the internal model principle in tracking a sequential cycloid trajectory to achieve video-rate atomic force microscope (AFM) imaging. To generate a sequential cycloid pattern, one axis of the nanopositioner traces a sinusoidal signal superimposed on a slow triangular wave. Discontinuities at turning points induce large peaks in the steady-state tracking error. To address this issue, a smooth trajectory is designed to reduce the magnitude of error by 60 nm compared with the triangular wave. This trajectory reduces the magnitude of error 10 times. The tracking controller includes the dynamics of the harmonic waveforms and the ramp signal as well as higher order harmonics of the scanning frequency, and an integrator to cope with the system nonlinearities at low frequencies. We perform experiments on a two degree of freedom microelectromechanical system nanopositioner at various scanning frequencies ranging from 500 to 2580 Hz within a scan area of 5 μm × 10 μm. The root-mean-square value of tracking error remains below 6.1 nm with a pitch size of 44.2 nm. We acquire time-lapse AFM images in contact mode at scan rates as high as 20 frames per second.**

***Index Terms*— Atomic force microscope (AFM), cycloid scan, internal model principle, nanopositioning, video rate.**

I. Introduction

IN RECENT years, we have observed a flurry of efforts to develop video-rate atomic force microscopy techniques to facilitate the study of observation of dynamic samples [1]–[4]. The conventional method of scanning in commercial atomic force microscopes (AFMs) is raster scanning whereby a lateral axis of the nanopositioner follows a triangular signal while the other axis tracks a ramp or a staircase signal [5]. Employing the raster trajectory, however, limits the achievable scan speed of the AFM. Since a triangular signal contains all the odd harmonics of its fundamental frequency, accurate tracking of a fast raster pattern is challenging due to the limited mechanical bandwidth and the highly resonant nature of the AFM nanopositioners. To avoid these complications, the raster frequency is often restricted to 1%–10% of the first resonance frequency of the scanner [6].

Manuscript received July 26, 2018; revised October 5, 2018; accepted October 23, 2018. Manuscript received in final form November 2, 2018. This work was supported by the UT-STARS Award. Recommended by Associate Editor X. Chen. *(Corresponding author: S. O. Reza Moheimani.)*

The authors are with the Erik Jonsson School of Engineering and Computer Science, The University of Texas at Dallas, Richardson, TX 75080 USA (e-mail: nastaran.nikooienejad@utdallas.edu; afshin.alipour@utdallas.edu; mohammad.maroufi@utdallas.edu; reza.moheimani@utdallas.edu).

Color versions of one or more of the figures in this paper are available online at http://ieeexplore.ieee.org.

Digital Object Identifier 10.1109/TCST.2018.2879939

In order to increase the imaging speed of the AFM, a number of approaches have been proposed. These range from using fast nanopositoners [7] and novel non-raster trajectories [8]–[10] to developing and incorporating high-bandwidth AFM cantilevers [11]. A review of recent developments in high-speed AFM imaging can be found in [4]. An important approach to increasing imaging speed in the AFM is to apply non-raster scan methods such as Lissajous [8], [12], [13], spiral [9], [14], and cycloid [10] which are based on harmonic waveforms. In the Lissajous pattern, the orthogonal axes of the nanopositioner are drived by sinusoidal references with fixed amplitude and slightly different frequency or phase. This trajectory makes the design of the controllers less challenging as the nanopositioner tracks narrowband sinusoidal references. However, this pattern retraces itself during one frame of the scan. The spiral method also employs sinusoidal references with varying amplitude in both axes. It can be implemented in constant angular velocity (CAV) with a fixed frequency [14] and constant linear velocity (CLV) [15], in which the frequency is progressively changed to maintain a constant velocity. Controller design for the latter method has proved to be challenging [15], [16]. The cycloid pattern utilizes sinusoidal references with a constant amplitude and frequency while the reference in one axis is superimposed on a slow ramp signal. Unlike the Lissajous method, this pattern displays only a progressive motion. Since the tracking amplitude and frequency are both constant, this method results in a more straightforward control design problem compared with the spiral pattern. In addition to imaging a complete frame, the cycloid method can potentially be implemented as part of feature tracking techniques for local imaging of string-like samples [17].

To achieve video-rate imaging, high-speed sequential scans of the sample are required. With cycloid and spiral patterns, the nanopositioner needs to move back and forth during sequential scans leading to inevitable discontinuities in the reference signal. These discontinuities can degrade the tracking performance of the nanopositioner and ultimately reduce the quality of AFM images. To address this problem, amplitude modulated waveforms are proposed and implemented for sequential spiral scanning in [18]. However, application of this method to cycloid scanning for video-rate AFM has not been reported yet.

Video-rate AFM requires high-bandwidth nanopositioning [19]–[22]. Microelectromechanical system (MEMS) nanopositioners are being investigated as promising alternatives to the

macroscale scanners for use in atomic force microscopy [23]. In [24], a high-bandwidth parallel kinematic MEMS nanopositioner is designed and tested as the scanning stage of an AFM. A two degree of freedom (2-DOF) serial kinematic MEMS nanopositioner is proposed in [25] featuring fast and slow axes with the resonance frequencies of 4.4 and 2.4 kHz, respectively. AFM imaging using spiral and Lissajous patterns are also demonstrated on MEMS nanopositioners in [14] and [26], respectively.

To achieve high-performance tracking of non-raster scan patterns, a number of control schemes have been developed. Model predictive controller (MPC) reported in [27] and the linear quadratic regulator (LQG) method in [28]–[30] are employed to track a spiral pattern. In [31], the phase-locked loop-based integral control scheme is presented to compensate the phase error between the displacements of two lateral axes in the tracking of the CAV spiral pattern. A Kalman filter-based controller is designed in [32] to track the Lissajous pattern at various frequencies ranging from 100 Hz to 5 kHz. Another control scheme is based on the internal model principle, which includes the dynamics of the reference signal to achieve asymptotically zero steady-state tracking error. This controller is an efficient method for tracking constant, ramp, and harmonic signals [33]. In addition, it allows to reject disturbances by augmenting their dynamics into the controller. In nanopositioning applications, the objective is to reduce the magnitude of the sensor noise, which is projected onto the output displacement of the nanopositioner, by limiting the closed-loop bandwidth while accurately tracking the reference signal [8]. Internal-model-based control can meet such requirements and was previously employed to implement a number of non-raster trajectories. Tracking Lissajous pattern in [8] and [26] and spiral trajectory in [14] are among the examples of such implementations.

In comparison to other control design methods such as LQG and MPC, the design and implementation of the internal-model-based controller are straightforward and intuitive. The MPC is computationally intensive, particularly when applied to video-rate imaging in the AFM. Furthermore, the performance of the LQG and the approximate internal model control in the tracking of the CLV spiral has been compared in [16] and the results show that the approximate internal model control outperforms the LQG method.

In this paper, video-rate AFM imaging is attempted in contact mode by employing the sequential cycloid scanning method. A 2-DOF MEMS nanopositioner, whose design and characterization are previously presented in [34] by our group, is used here as an in-plane scanner. A damping controller plus tracking controller are designed and implemented to augment damping and improve tracking performance of the nanopositioner. Furthermore, we take advantage of a method to shape the triangular signal to reduce the peak of tracking error during sequential scanning.

The rest of this paper continues as follows. The MEMS nanopositioner, its structure and characteristics are described in Section II. The cycloid pattern for sequential imaging is presented in Section III. Section IV details the controller design and reports the experimental outcomes. The results of AFM imaging at the highest rate of 20 fps are presented in Section V. Section VI concludes this paper.

II. MEMS Nanopositioner

In this section, the structure of the MEMS nanopositioner, its characterization, and the inner loop damping controller are presented. The scanning electron microscope (SEM) image of the 2-DOF MEMS nanopositioner used in this paper is shown in Fig. 1(a). The device comprises a scan table with the dimensions of 1.8 mm $\times$ 1.8 mm located at the center within a parallel kinematic mechanism allowing the stage to displace along the x- and y-axes. Electrostatic actuators are incorporated on each side to actuate the scan table back and forth along both axes. The force produced by the actuators is transferred to the stage via a shuttle beam and eight tethering beams as shown in the close-up view in Fig. 1(a). As a part of the suspension system along both axes, folded beam springs are designed and implemented. The device is fabricated from the standard SOIMUMPs microfabrication process [35]. During this process, the MEMS device is fabricated using a silicon-on-insulator wafer with 25 μm-thick single device layer from single-crystal silicon. The top surface of the device layer is n-doped at the beginning of the fabrication process. Patterning of the device layer is performed using deep reactive ion etching to realize the device mechanical structure. The device is then released by back-side etching of the substrate and buried oxide layer using dry and wet etch processes. Square-shaped gold features are also fabricated on the stage as shown in the close-up view in Fig. 1(a). These features are later used as reference patterns throughout the imaging experiments. Further details on the MEMS nanopositioner design and characterization are presented in [34].

A. Piezoresistive Displacement Sensor

In order to measure the displacement of the stage, bulk piezoresistive sensors are incorporated as shown in the close-up view in Fig. 1(a). The sensing mechanism is realized by using two pairs of slightly slanted silicon beams. These beams are anchored at one end and connected to the shuttle beam on the other. The other pair is covered with gold and connected to the electrical ground. As shown schematically in Fig. 1(b), through the horizontal motion of the shuttle beam, one tilted beam experiences axial compressive force, while the axial force along the other beam is tensile. Therefore, due to the piezoresistivity of the silicon, the electrical resistance of the tilted beams varies in opposite directions during the shuttle beam motion. The resistance variations are then converted to a voltage using a Wheatstone half-bridge and differentially amplified. Since this sensing mechanism relies on the bulk piezoresistivity of silicon, it eliminates the need for realization of highly doped regions on the mechanical flexures reducing the fabrication complexity and cost. The modeling and characterization of these sensors are further detailed in [23], [34], and [36].

B. Characterization

The MEMS device is characterized along both axes in time and frequency domains by implementing a linear actuation

This article has been accepted for inclusion in a future issue of this journal. Content is final as presented, with the exception of pagination.

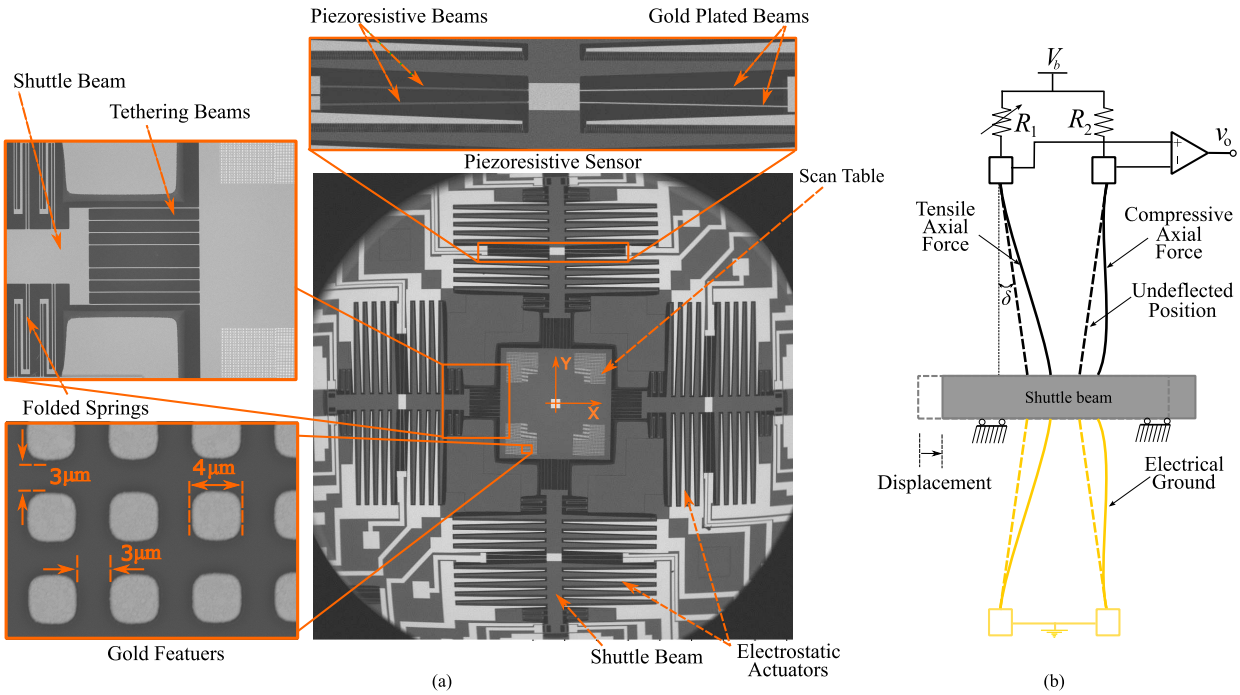

Fig. 1. (a) SEM image of the MEMS nanopositioner with the close-up views show various parts of the device. The scan table at the center has the dimensions of 1.8 mm × 1.8 mm. The dimensions of the square-shaped gold patterns on the stage are shown in the close-up view. (b) Schematic of the piezoresistive sensor while the shuttle beam undergoes a rectilinear displacement. The electrical resistance of the tilted beams and the external resistors R_1 and R_2 construct a Wheatstone half-bridge configuration. Here, the vertical length of the piezoresistive beams is 1 mm, $\delta = 0.86°$, and $R_{1,2} \sim 560\ \Omega$.

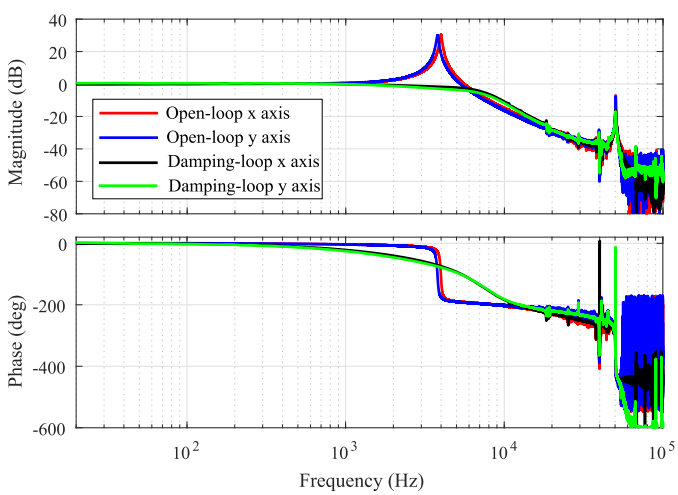

Fig. 2. Frequency response of the MEMS device along the orthogonal axes are compared in open loop and with the damping loop.

mechanism [24], [34]. During the characterization, the scan table displacement is obtained using a Polytec MSA-100-3D micro system analyzer. The device shows a displacement range up to 15 μm along both axes. In the time domain, a linear correlation is observed between the actuation voltage, the displacement of the scan table, and the corresponding sensors' output. These experimental data enabled us to calibrate the piezoresistive sensor. The calibration factors of 0.234 and 0.224 V/μm are obtained for the x- and y-axes, respectively.

The frequency response of the scan table along both axes is obtained by actuating the device using a wideband chirp signal and recording the sensors output. As shown in Fig. 2, the first resonance frequencies of the device are located at 3.9 and 3.8 kHz for the x- and y-axes, respectively. Resolution of the piezoresistive sensors is determined within the bandwidth of 30 kHz. Initially, their output noise is recorded with the sampling frequency of 62.5 kHz while an antialiasing filter (Stanford research SR650 low-noise filter) with a cutoff frequency of 30 kHz is also used in the path. Then, the sensors calibration factors are used to convert their root-mean-square (rms) noise to displacement. The 1-σ resolution of the sensors is obtained as 2.2 and 2.3 nm for the x- and y-axes, respectively.

C. Damping Controller

As shown in Fig. 2, an under damped characteristic is observable along each axis of the device. This lightly damped property renders the system prone to vibrations due to external disturbances and noise, which eventually deteriorate the system scanning performance. To alleviate this, an inner control loop controller (C_d) is employed to augment damping to the system for both axes

$$C_d(s) = \frac{5s}{s + 88\,000}. \tag{1}$$

The damping controller (C_d) used here is a high-pass filter that has only two parameters to tune and is implemented by an analog circuit described in [30], [32], and [37]. In order to keep the low-frequency gain of the system, the controller is implemented in the feedback path. The stability of the resulted damping loop is guaranteed according to negative imaginary systems theory [38]. The frequency response of

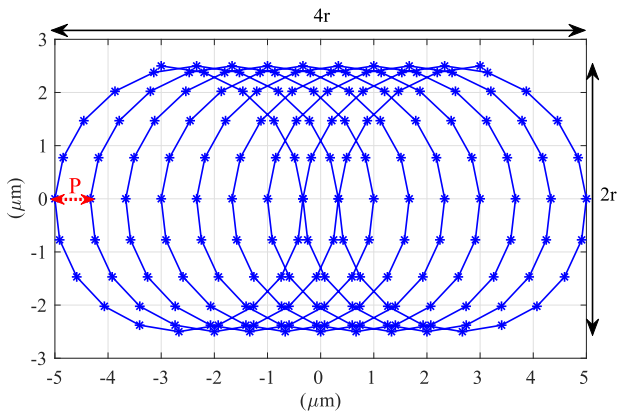

Fig. 3. Scanning pattern with cycloid trajectory in 5 μm × 10 μm scan area at $f = 10$ Hz.

the device with the inner damping loop is then obtained and compared with open loop as presented in Fig. 2. By using the damping loop, the resonant peaks are eliminated, and the −3 dB bandwidth of the device is consequently increased to about 4.6 kHz along both axes.

III. Cycloid Trajectory for Sequential Imaging

To generate the cycloid pattern shown in Fig. 3, the lateral axes of the scanner are forced to track the following waveforms:

$$x(t) = \alpha t + r\sin(\omega t), \quad y(t) = r\cos(\omega t) \tag{2}$$

where $\omega = 2\pi f$, f is the scanning frequency, r is the amplitude of sine wave, and α determines the slope of the ramp signal in the x-axis. Here, α is related to the pitch (P) through

$$\alpha = Pf. \tag{3}$$

The pitch in cycloid trajectory can be defined as the horizontal distance between two adjacent traverse lines, which is constant throughout the scan. By selecting a desired value for the pitch, the number of circles (N) required to travel through the scan area in a $2r \times 4r$ window is obtained as

$$N = \text{Round}\left(\frac{2r}{P} + \frac{1}{2}\right) \tag{4}$$

where N is rounded to the nearest integer. The scan time (T_{scan}) for capturing an image with a cycloid pattern is determined by

$$T_{\text{scan}} = \frac{(N+1)}{f}. \tag{5}$$

A comparison is now performed between cycloid, Lissajous, CAV spiral, and raster scanning methods in terms of their scan frequency and maximum tip velocity for fixed scan area, resolution, and scanning time as 44.63 $(\mu\text{m})^2$, 39.2 nm, and 50 msec, respectively. The scan area is what would be covered by the cycloid pattern over a 5 μm × 10 μm window.

TABLE I

Scan Frequency and Maximum Tip Velocity for Cycloid, Lissajous, CAV Spiral, and Raster Methods Considering Fixed Scan Area, Resolution, and Scan Time

Scanning method	Scan frequency (Hz)	Maximum velocity (mm/s)
Cycloid	2580	40.6
Lissajous	f_x = 3260 f_y = 3250	112.1
CAV Spiral	1903	45.5
Raster	2277	45.5

Considering the reference signals in (2) and $\upsilon = \sqrt{\dot{x}^2 + \dot{y}^2}$ as the tip velocity, the absolute maximum velocity in cycloid pattern is obtained as

$$\text{Cycloid}: \quad \upsilon_{\max} = \alpha + r\omega. \tag{6}$$

The maximum tip velocity in Lissajous [8], CAV spiral [15], and raster [39] trajectories are

$$\text{Lissajous}: \upsilon_{\max} = \sqrt{A_x^2\omega_x^2 + A_y^2\omega_y^2} \tag{7a}$$

$$\text{CAV spiral}: \upsilon_{\max} = \frac{2\pi r_f^2}{PT_{\text{scan}}} \tag{7b}$$

$$\text{Raster}: \upsilon = 2f_{\text{raster}} \times 4r \tag{7c}$$

where $A_x = 5$ μm, $A_y = 2.23$ μm, and $r_f = 3.77$ μm are specified from the scan area. The maximum tip velocity and the scan frequency related to each pattern are reported in Table I.

As given in Table I, to perform raster scanning with the same scan parameters as in cycloid, fast axis of the nanopositioner needs to follow a triangular signal at 2277 Hz. This requires a very fast nanopositioner, e.g., at least 20 kHz if the first four odd harmonics of the scan frequency are to be tracked [6]. Furthermore, we observe that the maximum tip velocity with a Lissajous pattern is far larger than the cycloid. Hence, operating the AFM with a Lissajous pattern requires a higher bandwidth z-axis nanopositioner. In CAV spiral, the tip velocity is maximum at the image periphery and it is approximately equal to that of the raster scan with the same imaging area.

A. Sequential Imaging

A conventional approach to obtain sequential imaging is superimposing a sinusoidal signal on a slow periodic triangular wave to construct the reference along each axis. We applied this reference to the x-axis, causing the nanopositoner to move back and forth along one side of the frame window capturing multiple frames. To evaluate the tracking performance of the MEMS nanoposoitioner during the sequential imaging, we take advantage of the estimated model of the damped system and the controller discussed in detail in Section IV. To achieve high frame rates, i.e., 20 fps, the scan frequency

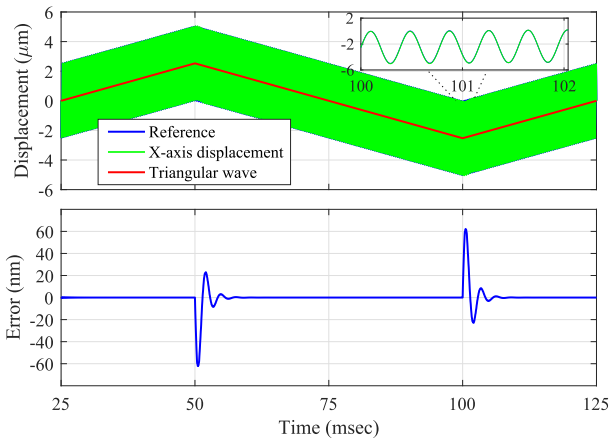

Fig. 4. Simulated tracking performance with triangular signal considering 5 μm × 10 μm scan area at $f = 2580$ Hz.

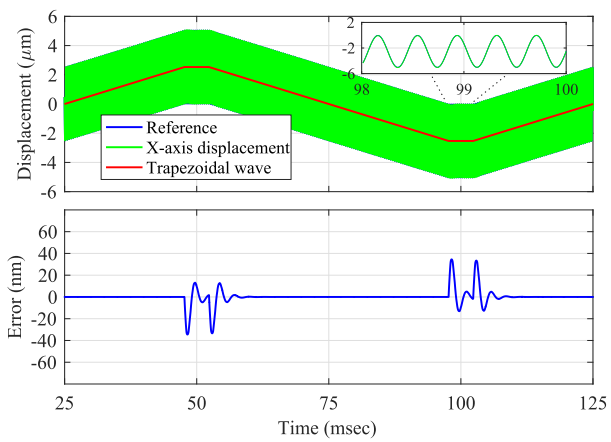

Fig. 5. Simulated tracking performance with trapezoidal signal considering 5 μm × 10 μm scan area at $f = 2580$ Hz.

is fixed at $f = 2580$ Hz while the scan area is set to 5 μm × 10 μm with a pitch of 39.2 nm. The frequency of slow triangular wave is 10 Hz.

Fig. 4 shows the reference signal for the x-axis and the simulated tracking error. We observe that the steady-state tracking error is zero owing to the tracking controller. However, the peak of transient error is 62 nm which is larger than the pitch. This makes some scan lines deviate from the reference pattern. As noted in Section IV-B, the system features a limited bandwidth with the combined damping and tracking controllers. Moreover, the dynamics of the x-axis closed-loop system shows a slightly under-damped behavior around 300 Hz due to the double integrator in the controller. Both these matters lead to an increase in tracking error at the sharp turning points. To address this issue, we shape the triangular signal in the time domain to obtain a trapezoidal signal with flat time-invariant sections and smoother discontinuous corners. In order to keep the frame rate as in the triangular case, we increase α in (2) to accomplish full-range scanning. Hence, the pitch in trapezoidal case is 43.2 nm, i.e., 10.28% larger. Fig. 5 depicts the reference along the x-axis with the trapezoidal signal and the simulated tracking error. Here, the error peak is reduced to 34.5 nm which is 44.35% smaller

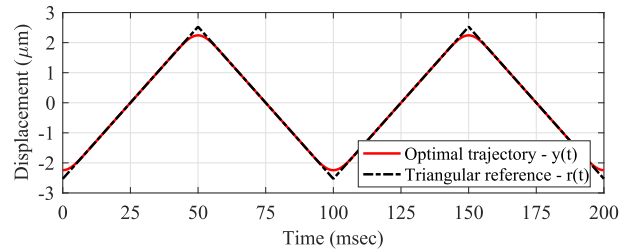

Fig. 6. Periodic triangular reference, $r(t)$, along with the optimal trajectory, $y(t)$.

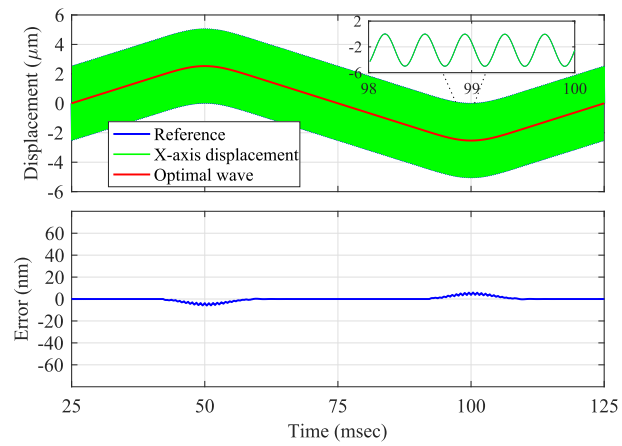

Fig. 7. Simulated tracking performance with optimal trajectory considering 5 μm × 10 μm scan area at $f = 2580$ Hz.

than the previous case. Although the error peak is less than the pitch value, some artifacts will appear in the image because in-plane displacement diverges from the reference. To decrease the peak of tracking error such that it becomes negligible compared to the pitch, we take advantage of the method described in [40] to further smoothen the sharp turning points. Considering a periodic triangular trajectory $r(t)$, one approach is based on keeping the linear range of the trajectory unchanged while shaping the sharp discontinuities to obtain a new smooth trajectory, $y(t)$, as shown in Fig. 6. This can be cast as a linearly constrained convex quadratic optimization problem (8) to minimize a frequency-domain quadratic cost, $x^T H x$. That is,

$$y = \arg\min_{x} x^T H x \quad \text{subject to } x_k = r_k, \quad k \in S \tag{8}$$

where $x, r \in \mathbb{R}^{N\times 1}$, and $H \in \mathbb{R}^{N\times N}$. We define $S : \{k \mid r_k < |\beta| r_{\max}\}$ as a set of sample indices for which the samples of $r(t)$ are within the linear range of triangular signal. As shown in the Appendix, H is chosen to minimize the power of $r(t)$ beyond a certain harmonic and β is selected as 0.7 to maintain the maximum scan range.

As depicted in Fig. 7, applying the optimal trajectory instead of the triangular signal reduces the peak of tracking error dramatically to 5.8 nm while keeping the steady-state error zero. Consequently, we employ this trajectory in our experiments to improve the tracking performance. Note that as we keep the scan range and frame rate constant, there is a 12.77% increase in the pitch relative to the triangular case.

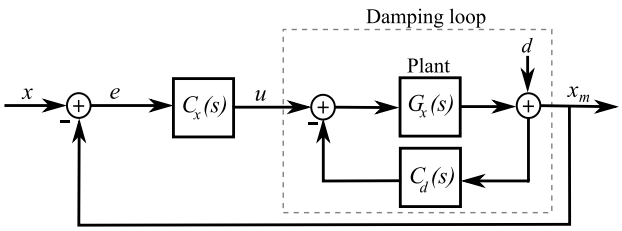

Fig. 8. Block diagram of the control system for the x-axis. The same scheme is used for the y-axis.

IV. Internal-Model-Based Control for Sequential Cycloid Trajectory

In this section, we present the controller design procedure to track a sequential cycloid trajectory. The objective is to track the reference signal at a high scanning frequency; thus, a linear controller with a minimum number of poles is desired. Among different linear controllers, a conventional PID can be a candidate. However, implementing the derivative term in a feedback loop is problematic in the presence of sensor readout noise. In addition, the PID scheme cannot track a sine wave without leaving a sinusoidal error at the same frequency, even though the magnitude of the error can be minimized by tuning the PID gains. As a result, a controller based on the internal model principle can be an alternative for high-precision tracking. A superior advantage of this controller is reducing the steady-state tracking error remarkably while keeping the closed-loop bandwidth low [8] resulting in a very low sensor noise footprint on the required position of the scanner.

Here, controller design starts with the simplest form of the controller, i.e., by including just the model of reference signals in the tracking controller. In the next step, other modes are added to the controller to improve the tracking performance in presence of harmonic disturbances due to the nonlinear nature of the piezoelectric actuators. We designed the controller for a number of scan frequencies ranging from 500 to 2580 Hz. The block diagram of the closed-loop x-axis system is shown in Fig. 8. The same scheme is used to control the y-axis.

A. Initial Controllers

As pointed out earlier, the x-axis follows a sine wave superimposed on an optimal triangular signal, while the stage needs to just follow a cosine wave along the y-axis. Initially, the controllers for each axis are designed for the fundamental frequency of the sinusoidal signals as follows:

$$C_{x_i} = \frac{A_{x_i}(s)}{B_{x_i}(s)} \tag{9}$$

$$C_{y_i} = \frac{A_{y_i}(s)}{B_{y_i}(s)} \tag{10}$$

where $A_{x_i}(s)$, $B_{x_i}(s)$, $A_{y_i}(s)$, and $B_{y_i}(s)$ are the polynomials defined as

$$A_{x_i}(s) = a_4 s^4 + a_3 s^3 + a_2 s^2 + a_1 s + a_0 \tag{11}$$

$$B_{x_i}(s) = s^2(s^2 + \omega^2) \tag{12}$$

$$A_{y_i}(s) = b_2 s^2 + b_1 s + b_0 \tag{13}$$

$$B_{y_i}(s) = (s^2 + \omega^2) \tag{14}$$

where $\omega = 2\pi f$, and f is the scan frequency. In order to have more flexibility to assign the desired closed-loop poles, the controllers are considered to be proper. This consequently adds a proportional term to the controllers. Assuming the following transfer functions for the damped system:

$$G_x = \frac{N_x(s)}{D_x(s)} \tag{15}$$

$$G_y = \frac{N_y(s)}{D_y(s)}. \tag{16}$$

The characteristic polynomial of the closed-loop system can be obtained as

$$E_x(s) = B_{x_i}(s)D_x(s) + A_{x_i}(s)N_x(s) \tag{17}$$

$$E_y(s) = B_{y_i}(s)D_y(s) + A_{y_i}(s)N_y(s). \tag{18}$$

The coefficients of polynomials in (11)–(14) can be determined by the pole placement from the characteristic polynomials on the left-hand side of (17) and (18) based on the closed-loop poles. The desired closed-loop poles were selected to achieve reasonably low settling times, and small closed-loop bandwidths, while minimizing the peak in the steady-state tracking error along the x-axis at the turning points. The desired closed-loop system poles, as well as the closed-loop gain and phase margins with this controller (at $f = 2580$ Hz) are reported in Table II.

We next conduct an experiment to evaluate tracking performance of sequential cycloid pattern at $f = 2580$ Hz. Fig. 9(a) and (b) depicts the time domain and Fast Fourier Transform (FFT) of steady-state tracking error along the x- and y-axes. For the sake of clarity, the tracking error for only six consecutive scans is depicted. The rms values of tracking error are 21.4 and 5.6 nm in the x- and y-axes, respectively. The actuation in the x-axis is composed of a high-frequency sinusoid and a low-frequency optimal triangular trajectory. In addition, the force can be practically a nonlinear (quadratic) function of actuation voltage even a linear actuation mechanism is used [41]. Thus, the tracking error in the x-axis, shown in Fig. 9(a), is a multiplication of the two actuation reference signals and its large amplitude is due to the dominant higher harmonic of the sinusoid, i.e., $f = 5160$ Hz in the FFT of tracking error in Fig. 9(b). The tracking error signal of the y-axis in Fig. 9(a) shows a pattern corresponding to the low-frequency optimal triangular signal in the x-axis. This pattern reveals the presence of cross coupling between the two orthogonal axes and it is notable as low-frequency harmonics in the frequency domain as in Fig. 9(b). In addition, there are two other dominant components in the FFT of error signals as depicted in Fig. 9(b). These components, observable in both axes, are the second and third harmonics of the scan frequency generated due to the system nonlinearities.

B. Final Controllers

If we consider the plant as a linear time-invariant system, the resulting steady-state tracking error is zero just by employing the initial controllers. However, the presence of higher order harmonics indicates that the plant has some nonlinearities. In addition, a slight level of cross coupling is

This article has been accepted for inclusion in a future issue of this journal. Content is final as presented, with the exception of pagination.

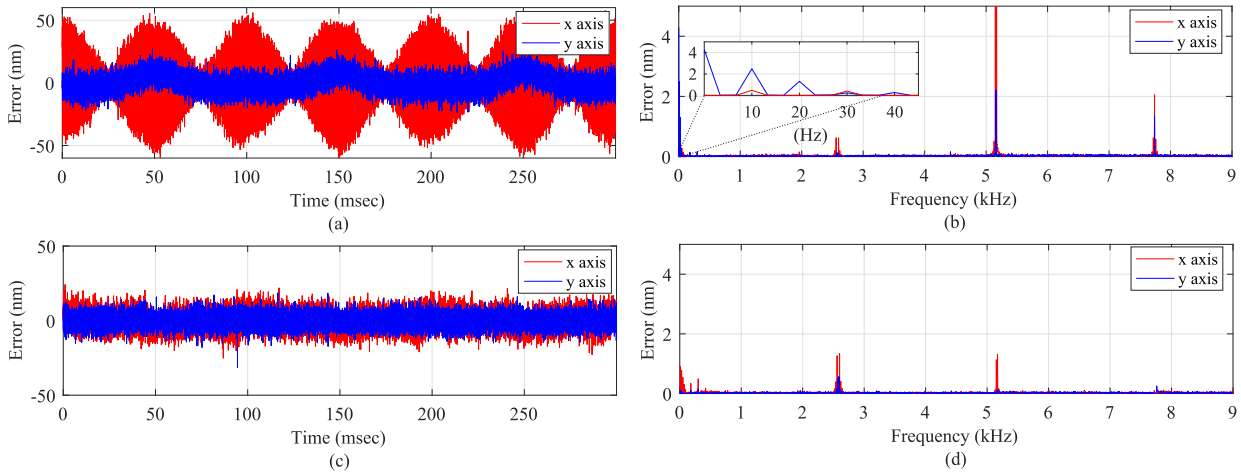

Fig. 9. x- and y-axes tracking error with the initial controllers in (a) time domain and (b) FFT. Tracking error with the final controllers for the x- and y-axes in (c) time domain and (d) FFT. For the sake of clarity, the y-axis range in FFT figures is adjusted to be equal, while the maximum amplitude in (b) is about 10 nm. The scanning is performed in 5 μm × 10 μm area at $f = 2580$ Hz.

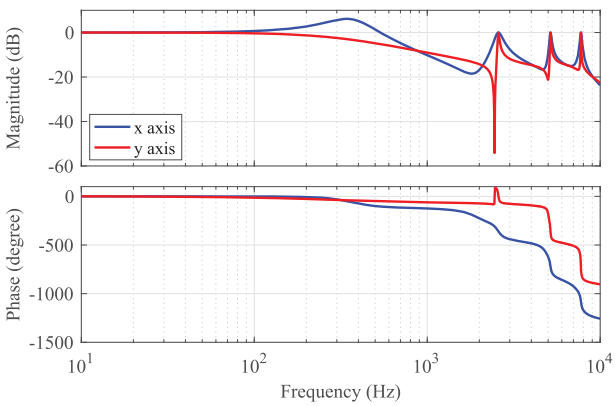

Fig. 10. Simulated frequency response of closed-loop system with the final controllers at $f = 2580$ Hz.

also observed between the two orthogonal axes of motion. To alleviate the first issue, we add pure imaginary poles at the second and third harmonics of the scan frequency to the controllers. In addition, an integrator can be incorporated in the controllers to address the second problem. However, as the x-axis controller already includes a double integrator to follow the ramp signal, we just need to add a pole at the origin to the y-axis controller to eliminate the error induced by the cross coupling. The resulting controllers are

$$C_{x_f} = \frac{\sum_{\ell=0}^{8} a_\ell s^\ell}{s^2(s^2+\omega^2)(s^2+(2\omega)^2)(s^2+(3\omega)^2)} \tag{19}$$

$$C_{y_f} = \frac{\sum_{\ell=0}^{7} a_\ell s^\ell}{s(s^2+\omega^2)(s^2+(2\omega)^2)(s^2+(3\omega)^2)}. \tag{20}$$

We select the desired poles to reject the dominant higher harmonics of scan frequency. Table II tabulates the desired closed-loop poles, gain, and phase margins for scan frequencies ranging from 500 to 2580 Hz and the settling time of step response within 2% of its final value. Fig. 10 shows the simulated frequency response of the closed-loop system for both axes.

We also repeat the tracking experiment with the final controllers. Fig. 9(c) and (d) plots the x- and y-axes tracking errors in the time and frequency domains. This controller satisfactorily mitigates the effect of undesirable harmonics. Moreover, the rms values of error for the x- and y-axes are reduced to 6.1 and 4.3 nm, respectively. These low rms values indicate that the tracking controllers effectively track the reference signals. The rms value of the y-axis tracking error remains below 4.4 nm by increasing the scanning frequency; however, the error rms value along the x-axis increases from 4.6 nm at 500 Hz to 6.1 nm at 2580 Hz. This is most likely due to the increase in the triangular signal frequency and tracking error peaks at the turning points. In Fig. 9(d), we observe that a number of small harmonics around those included in the controller are amplified. These harmonics are inevitable because the controller has undamped behavior around them.

C. Experiments

All experiments involved a digital signal processing system (dSPACE MicroLabBox) operating at a sampling frequency of 80 kHz. We performed sequential cycloid tracking with triangular, trapezoidal, and optimal signals at scan frequencies ranging from 500 to 2580 Hz in open loop, with a damping controller, and finally in a closed loop with a combination of damping and tracking controllers. The selected scan frequencies correspond to the imaging frame rate of 3.8–20 fps. Here, we report the experimental results for the highest frame rate while tracking performance at other scan frequencies are reported in Table II.

To investigate the improvement achieved with the tracking controller, the tracking performance is compared with the open loop and the damping loop cases. To have a fair comparison, the gain is adjusted to unity at the scan frequency of 2580 Hz. Setting the gain to unity for the x-axis, however, is challenging since the reference signal includes both low- and high-frequency components for which the plant has different gains. Therefore, we only compare the tracking performance for the y-axis as shown in Fig. 11. It is evident that the system is unable to follow the reference signal accurately in open loop

TABLE II

DESIRED CLOSED-LOOP POLES AT VARIOUS SCANNING FREQUENCIES, PHASE, AND GAIN MARGINS OF EACH CONTROLLER AND THE SETTLING TIME OF THE CLOSED-LOOP STEP RESPONSE WITHIN 2% OF ITS FINAL VALUE

Controller	**Desired Closed-loop poles** $/2\pi$ (kHz)	**Gain Margin** (dB)	**Phase Margin** (degree)	**Settling Time** (msec)	**RMS – Error** (nm)
	f = 500 Hz **and frame rate = 3.8** fps				
C_{x_f}	$-2.6755 \pm 6.6865i$, -3.2785, $-0.0486 \pm 1.4668i$, $-0.0527 \pm 0.9609i$, $-0.0261 \pm 0.4522i$, -0.5078, -0.1951	7.74	55	14.2	4.6
C_{y_f}	$-2.2646 \pm 7.1761i$, -3.5783, $-0.0248 \pm 1.4842i$, $-0.0834 \pm 0.9594i$, $-0.0143 \pm 0.4928i$, -0.2828	15.21	99	11.2	4.2
	f = 1000 Hz **and frame rate = 7.7** fps				
C_{x_f}	$-2.2736 \pm 6.6762i$, -3.0932, $-0.0660 \pm 2.9508i$, $-0.1093 \pm 1.9073i$, $-0.1180 \pm 0.8336i$, -1.1294, -0.1848	9.8	60	4.8	4.6
C_{y_f}	$-2.2823 \pm 7.1073i$, -3.2817, $-0.1144 \pm 2.9450i$, $-0.1140 \pm 1.9681i$, $-0.0196 \pm 0.9941i$, -0.3056	15.28	87	5.2	4.2
	f = 1600 Hz **and frame rate = 12.4** fps				
C_{x_f}	$-2.1003 \pm 6.6356i$, $-0.3404 \pm 4.6380i$, -2.8501, $-0.1823 \pm 3.1449i$, $-0.1810 \pm 1.4924i$, $-0.5439 \pm 0.2012i$	9.14	52	2.4	4.9
C_{y_f}	$-2.3091 \pm 7.0890i$, $-0.0657 \pm 4.7711i$, -3.2087, $-0.1714 \pm 3.1464i$, $-0.0249 \pm 1.5934i$, -0.3096	16.11	82	3.5	4.4
	f = 2000 Hz **and frame rate = 15.5** fps				
C_{x_f}	$-2.1398 \pm 6.7139i$, $-0.1150 \pm 5.9574i$, $-0.2783 \pm 3.8859i$, -3.3638, $-0.2496 \pm 1.9253i$, $-0.3084 \pm 0.2996i$	10.80	53	2.4	4.8
C_{y_f}	$-2.3527 \pm 7.0777i$, $-0.0819 \pm 5.9744i$, $-0.1105 \pm 3.9692i$, -3.2165, $-0.0266 \pm 1.9927i$, -0.3134	15.16	79	3.5	4.4
	f = 2580 Hz **and frame rate = 20** fps				
C_{x_i}	$-2.2760 \pm 6.6957i$, $-0.2705 \pm 2.4249i$, -3.3095, -0.6593, -0.4795	13.23	63	17	21.4
C_{y_i}	$-2.3359 \pm 7.2338i$, $-0.0942 \pm 2.5532i$, -3.7875	16.96	98	3.8	6.9
C_{x_f}	$-0.0931 \pm 7.7416i$, $-0.0700 \pm 5.1517i$, $-2.6276 \pm 6.6903i$, -3.5022, $-0.1430 \pm 2.5638i$, $-0.1145 \pm 0.3509i$	16.44	32	5.6	6.1
C_{y_f}	$-0.0197 \pm 7.7390i$, $-2.6729 \pm 6.9797i$, $-0.0267 \pm 5.1557i$, -2.8950, $-0.0272 \pm 2.5743i$, -0.3355	17.96	82	2.6	4.4

and with a damping controller. The large phase lag between the actual trajectory and the sensor output signal in open loop and damping loop is completely eliminated in the closed loop. The rms values in open loop, damping loop, and closed loop are 576.9,1850.0, 4.3 nm, respectively, proving a considerable improvement in the tracking error which is achieved by using closed-loop control scheme.

D. Cycloid Trajectory Tracking

As shown by the simulation results in Section III, superimposing the optimal signal in the x-axis reduces the sharp peaks of tracking error remarkably. Here, we perform the experiment in closed loop at the highest scan frequency, i.e., $f = 2580$ Hz while applying the triangular, trapezoidal, and optimal signal superimposed by the sinusoid in the x-axis. The scanning time and frequency are fixed throughout the experiment. The resulting x-axis tracking error is depicted in Fig. 12. To visualize the deterministic error clearer, we removed the high-frequency components by incorporating a low-pass sixth-order Butterworth filter with cutoff frequency of 1500 Hz. As shown in Fig. 12, using the conventional triangular signal in the x-axis generates 66.5 nm peak in the tracking error around the turning points which is reduced to about 38.0 nm with the trapezoidal signal. Although the discontinuities in the trapezoidal signal are smoother than the triangular reference, the tracking error is still relatively

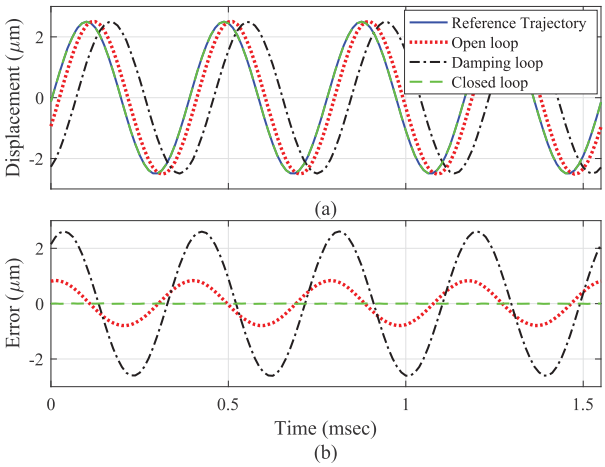

Fig. 11. (a) Tracking performance of open loop, damping loop, and closed loop along the y-axis in scanning a 5 μm × 10 μm area at $f = 2580$ Hz. (b) y-axis tracking error in open loop, damping loop, and closed loop.

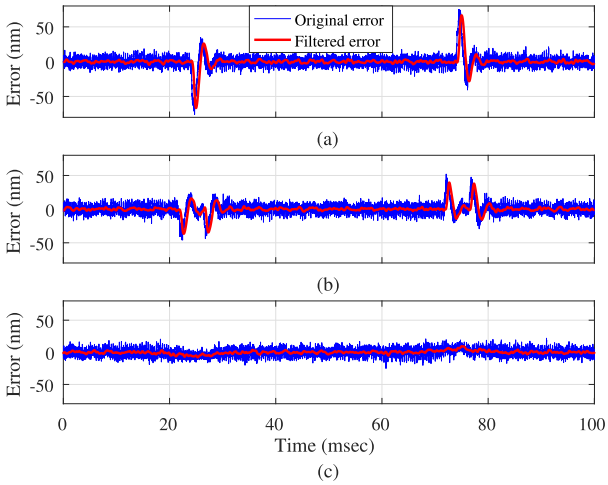

Fig. 12. x-axis tracking error of three successive frames at $f = 2580$ Hz when a sinusoid is superimposed on (a) triangular, (b) trapezoidal, and (c) optimal trajectory.

large at the turning points. In addition, as shown in Fig. 5, the trapezoidal signal is flat for a certain period of time which leads to repeated and redundant scan lines in specific parts of the scan area. The use of the alternative optimal trajectory, on the other hand, nearly eliminates the peak of tracking error.

The cycloid scanning pattern and the actual trajectory at $f = 2580$ Hz by incorporating the final controllers and the optimal signal are depicted in Fig. 13(a). As shown in Fig. 13(b), both controllers track the references in the x- and y-axes very well and the profile of tracking error explains the positioning accuracy of the nanopositioner.

V. AFM Imaging

To obtain AFM images at video rate, the MEMS nanopositioner is used as a scanning stage in an AFMWorkshop TT-AFM. Fig. 14 demonstrates the experimental setup including the AFM, MEMS nanopositioner, and a custom-designed printed circuit board. As the scan samples, the periodic gold patterns on the scan table with the dimension of 4 μm × 4 μm × 0.5 μm are used. The scan area is 5 μm × 10 μm and the scan frequency is $f = 2580$ Hz, while the imaging data are recorded at the sampling rate of 1 MHz. 3-D images are constructed from the cantilever deflection signal and xy-displacement provided by the piezoresistive sensors of the nanopositioner. Since the limited bandwidth of the z-axis positioner in commercial AFMs impedes high-speed scanning, we operated the system in constant-height contact mode. The scanning is performed by a contact-mode cantilever with a resonance frequency of 27 kHz and a stiffness of approximately 0.32 N/m. The stiffness of the cantilever is estimated based on its resonance frequency and the given characteristics in the data sheet.

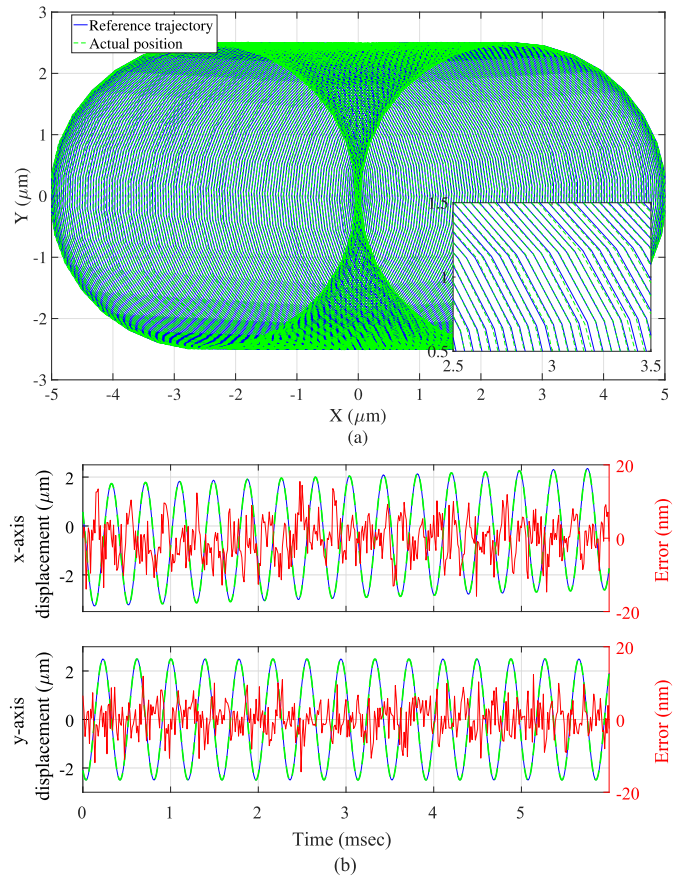

Fig. 13. (a) Reference pattern and the actual tracking after implementing the final controller designed at $f = 2580$ Hz. (b) Close-up views of tracking performance at $f = 2580$ Hz along the x- and y-axes. (—- reference, —— actual position, —- error).

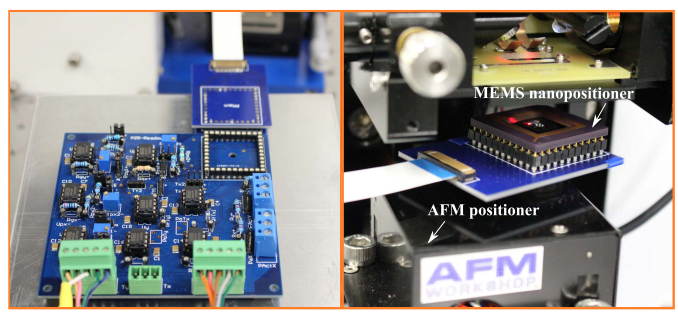

Fig. 14. Experimental setup for AFM imaging.

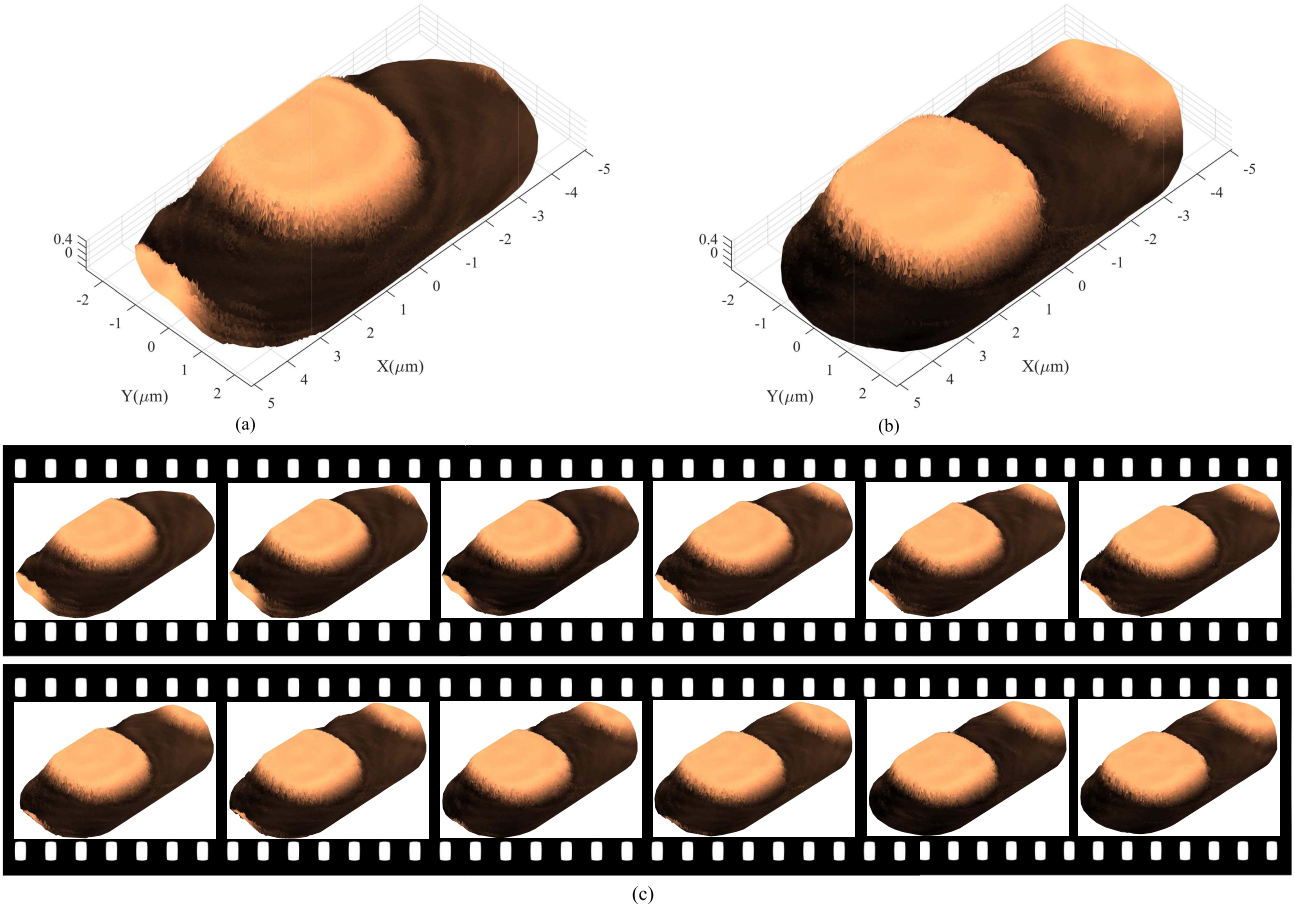

Fig. 15. (a) 3-D AFM image of gold features. (b) 3-D AFM image of gold features after passing 12 consecutive frames. (c) Video frames (from top-left to bottom-right) captured from 12 successive AFM images of slowly moving sample in constant-height contact mode. The scan area is 5 μm × 10 μm and the video frame rate is 20 fps.

The 3-D topography of the gold features at two different scanning intervals are depicted in Fig. 15(a) and (b). The imaging was performed while the entire MEMS nanopositioner was also slowly moved in the xy plane using the embedded nanopositioner of the AFM. During this test, the slow movement of the features beneath the AFM probe is observable due to the video-rate imaging. The movement is accomplished by implementing raster scanning with the built-in positioner of the AFM at the lowest possible raster frequency, i.e., 0.6 Hz. Fig. 15(c) shows a series of video frames at the frame rate of 20 fps achieved by the sinusoidal frequency of 2580 Hz. The images demonstrate a good tracking performance. However, we observe artifacts at the edge of gold features due to the AFM cantilever vibrations as it undergoes a sharp transition in features height. Operating the system in constant-force contact mode will resolve this issue. However, the commercial AFM used in these experiments cannot deliver the required high z-axis bandwidth, limiting us to constant-height mode only.

VI. Conclusion

A sequential cycloid pattern is presented to acquire video-rate AFM imaging. We implemented an internal-model-based controller on a 2-DOF MEMS nanopositioner to achieve high-performance tracking. The controller incorporates internal models of the reference signals plus a pair of pure imaginary poles at the second and third harmonics of fundamental scan frequency to reject unwanted signals due to the plant nonlinearities. The tracking error peak was reduced remarkably by exploiting an optimization method to smoothen the sharp corners in the triangular wave. The experimental results revealed that the peak of tracking error is decreased by 60 nm as a result of using the optimal trajectory. Finally, we performed time-lapse AFM imaging at 20 fps by using a MEMS nanopositioner within a TT-AFM and moving the sample slowly.

Appendix

As discussed in [40], consider r as a vector of the samples of a triangular signal $r(t)$ at $t = nT_s$ over one period T

$$r = \begin{bmatrix} r_0 \\ r_1 \\ \vdots \\ r_{N-1} \end{bmatrix} = \begin{bmatrix} r(0) \\ r(T_s) \\ \vdots \\ r((N-1)T_s) \end{bmatrix} \quad r \in \mathbb{R}^{N\times 1} \tag{21}$$

where T_s is the sampling period and N is the number of samples in one period. From signal processing perspective [42],

c_k denotes the Fourier series coefficients of a periodic discrete signal r as

$$c_k = \frac{1}{N}\sum_{n=0}^{N-1} r_n e^{-jn\frac{2\pi k}{N}}. \tag{22}$$

Here, c can be written in a vector notation as

$$c = \frac{1}{N}Er \tag{23}$$

where $c \in \mathbb{R}^{N\times 1}$ and $E \in \mathbb{R}^{N\times N}$ is

$$E = \begin{bmatrix} 1 & 1 & 1 & \dots & 1 \\ 1 & e^{-j\frac{2\pi 1}{N}} & e^{-j2\frac{2\pi 1}{N}} & \dots & e^{-j(N-1)\frac{2\pi 1}{N}} \\ 1 & e^{-j\frac{2\pi 2}{N}} & e^{-j2\frac{2\pi 2}{N}} & \dots & e^{-j(N-1)\frac{2\pi 2}{N}} \\ \vdots & \vdots & \vdots & \ddots & \vdots \\ 1 & e^{-j\frac{2\pi(N-1)}{N}} & e^{-j2\frac{2\pi(N-1)}{N}} & \dots & e^{-j(N-1)\frac{2\pi(N-1)}{N}} \end{bmatrix}. \tag{24}$$

Using the Parseval's identity, the power of r is

$$P_r = \sum_{k=0}^{N-1} |c_k|^2 = c^* c \tag{25}$$

and by substituting (23) in (25), we have

$$P_r = \frac{1}{N^2} r^T E^* E r. \tag{26}$$

By defining W as a window to select the Fourier coefficients at which the power should be minimized, the frequency weighted power is

$$P_r^W = \frac{1}{N^2} r^T E^* W E r \tag{27}$$

where $W = \mathrm{diag}(Q)$ and Q is

$$Q = \begin{cases} 0, & k \in [0, 1, \dots, K] \\ 1, & k \in [K+1, \dots, N-K-1] \\ 0, & k \in [N-K, \dots, N-1] \end{cases} \tag{28}$$

where K denotes the harmonic beyond which the frequency power is minimized. According to the Fourier series of a triangle wave, the contribution of the first four odd harmonics is more than the higher harmonics. Here, we select K as 9 to keep dominant harmonics of signal. Consequently, the weighting matrix H in (8) is obtained as

$$H = \frac{1}{N^2} E^* W E. \tag{29}$$

References

[1] B. Hartman, S. Andersson, W. Nagel, and K. Leang, "Non-raster high-speed AFM imaging of biopolymers," *Biophysical J.*, vol. 112, no. 3, p. 587a, Feb. 2017.

[2] N. Kotani, R. Kumaresan, Y. Kawamoto-Ozaki, T. Morii, and T. Okada, "High-speed AFM reveals advanced details on dynamic behavior of antibody," *Biophys. J.*, vol. 112, no. 3, p. 587a, Feb. 2017.

[3] T. Ando, T. Uchihashi, and N. Kodera, "High-speed AFM and applications to biomolecular systems," *Annu. Rev. Biophys.*, vol. 42, pp. 393–414, 2013.

[4] T. Ando, "High-speed atomic force microscopy coming of age," *Nanotechnology*, vol. 23, no. 6, p. 062001, Feb. 2012.

[5] Y. K. Yong, S. O. R. Moheimani, B. J. Kenton, and K. Leang, "Invited review article: High-speed flexure-guided nanopositioning: Mechanical design and control issues," *Rev. Sci. Instrum.*, vol. 83, no. 12, p. 121101, 2012.

[6] S. Devasia, E. Eleftheriou, and S. O. R. Moheimani, "A survey of control issues in nanopositioning," *IEEE Trans. Control Syst. Technol.*, vol. 15, no. 5, pp. 802–823, Sep. 2007.

[7] Y. K. Yong and K. K. Leang, "Mechanical design of high-speed nanopositioning systems," in *Nanopositioning Technologies*. Cham, Switzerland: Springer, 2016, pp. 61–121.

[8] A. Bazaei, Y. K. Yong, and S. O. R. Moheimani, "High-speed lissajous-scan atomic force microscopy: Scan pattern planning and control design issues," *Rev. Sci. Instrum.*, vol. 83, no. 6, p. 063701, Jun. 2012.

[9] I. A. Mahmood, S. O. R. Moheimani, and B. Bhikkaji, "A new scanning method for fast atomic force microscopy," *IEEE Trans. Nanotechnol.*, vol. 10, no. 2, pp. 203–216, Mar. 2011.

[10] Y. K. Yong, S. O. R. Moheimani, and I. Petersen, "High-speed cycloid-scan atomic force microscopy," *Nanotechnology*, vol. 21, no. 36, p. 365503, Aug. 2010.

[11] T. Ando, N. Kodera, E. Takai, D. Maruyama, K. Saito, and A. Toda, "A high-speed atomic force microscope for studying biological macromolecules," *Proc. Nat. Acad. Sci. USA*, vol. 98, no. 22, pp. 12468–12472, Oct. 2001.

[12] T. Tuma, J. Lygeros, V. Kartik, A. Sebastian, and A. Pantazi, "High-speed multiresolution scanning probe microscopy based on lissajous scan trajectories," *Nanotechnology*, vol. 23, no. 18, p. 185501, May 2012.

[13] Y. K. Yong, A. Bazaei, and S. O. R. Moheimani, "Video-rate lissajous-scan atomic force microscopy," *IEEE Trans. Nanotechnol.*, vol. 13, no. 1, pp. 85–93, Jan. 2014.

[14] A. Bazaei, M. Maroufi, A. G. Fowler, and S. O. R. Moheimani, "Internal model control for spiral trajectory tracking with MEMS AFM scanners," *IEEE Trans. Control Syst. Technol.*, vol. 24, no. 5, pp. 1717–1728, Sep. 2016.

[15] D. Ziegler, T. R. Meyer, A. Amrein, A. L. Bertozzi, and P. D. Ashby, "Ideal scan path for high-speed atomic force microscopy," *IEEE/ASME Trans. Mechatronics*, vol. 22, no. 1, pp. 381–391, Feb. 2017.

[16] A. Bazaei, M. Maroufi, and S. O. R. Moheimani, "Tracking of constant-linear-velocity spiral trajectories by approximate internal model control," in *Proc. IEEE Conf. Control Technol. Appl.*, Mauna Lani, HI, USA, Aug. 2017, pp. 129–134.

[17] J. L. Worthey and S. B. Andersson, "Local circular scanning for autonomous feature tracking in AFM," in *Proc. Amer. Control Conf. (ACC)*, Jul. 2015, pp. 3490–3495.

[18] A. Bazaei, Y. K. Yong, and S. O. R. Moheimani, "Combining spiral scanning and internal model control for sequential AFM imaging at video rate," *IEEE/ASME Trans. Mechatronics*, vol. 22, no. 1, pp. 371–380, Feb. 2017.

[19] B. J. Kenton and K. K. Leang, "Design and control of a three-axis serial-kinematic high-bandwidth nanopositioner," *IEEE/ASME Trans. Mechatronics*, vol. 17, no. 2, pp. 356–369, Apr. 2012.

[20] K. Cai, Y. Tian, L. Cui, Z. Yang, and D. Zhang, "Design and stiffness analysis of a XYZ scanning stage," in *Proc. Int. Conf. Manipulation, Autom. Robot. Small Scales (MARSS)*, Jul. 2016, pp. 1–6.

[21] C. Yang, J. Yan, M. Dukic, N. Hosseini, J. Zhao, and G. E. Fantner, "Design of a high-bandwidth tripod scanner for high speed atomic force microscopy," *Scanning*, vol. 38, no. 6, pp. 889–900, Nov. 2016.

[22] M. Rana, H. R. Pota, and I. R. Petersen, "Improvement in the imaging performance of atomic force microscopy: A survey," *IEEE Trans. Autom. Sci. Eng.*, vol. 14, no. 2, pp. 1265–1285, Apr. 2017.

[23] M. Maroufi, A. G. Fowler, and S. O. R. Moheimani, "MEMS for nanopositioning: Design and applications," *J. Microelectromech. Syst.*, vol. 26, no. 3, pp. 469–500, Jun. 2017.

[24] M. Maroufi, A. Bazaei, and S. O. R. Moheimani, "A high-bandwidth MEMS nanopositioner for on-chip AFM: Design, characterization, and control," *IEEE Trans. Control Syst. Technol.*, vol. 23, no. 2, pp. 504–512, Mar. 2015.

[25] M. Maroufi, A. G. Fowler, and S. O. R. Moheimani, "MEMS nanopositioner for on-chip atomic force microscopy: A serial kinematic design," *IEEE J. Microelectromech. Syst.*, vol. 24, no. 6, pp. 1730–1740, Dec. 2015.

[26] M. Maroufi, A. G. Fowler, A. Bazaei, and S. O. R. Moheimani, "High-stroke silicon-on-insulator MEMS nanopositioner: Control design for non-raster scan atomic force microscopy," *Rev. Sci. Instrum.*, vol. 86, no. 2, p. 023705, Feb. 2015.

[27] M. Rana, H. Pota, and I. Petersen, "Performance of sinusoidal scanning with MPC in AFM imaging," *IEEE/ASME Trans. Mechatronics*, vol. 20, no. 1, pp. 73–83, Feb. 2015.

[28] H. Habibullah, H. Pota, and I. Petersen, "High-speed spiral imaging technique for an atomic force microscope using a linear quadratic Gaussian controller," *Rev. Sci. Instrum.*, vol. 85, no. 3, p. 033706, Mar. 2014.

[29] H. Habibullah, H. R. Pota, and I. R. Petersen, "A novel control approach for high-precision positioning of a piezoelectric tube scanner," *IEEE Trans. Autom. Sci. Eng.*, vol. 14, no. 1, pp. 325–336, Jan. 2017.

[30] A. Bazaei, M. Maroufi, and S. O. R. Moheimani, "Tracking control of constant-linear-velocity spiral reference by LQG method," *IFAC-PapersOnLine*, vol. 50, no. 1, pp. 15568–15573, Jul. 2017.

[31] H. Habibullah, H. Pota, and I. Petersen, "Phase-locked loop-based proportional integral control for spiral scanning in an atomic force microscope," *IFAC Proc. Vol.*, vol. 47, no. 3, pp. 6563–6568, 2014.

[32] M. G. Ruppert, M. Maroufi, A. Bazaei, and S. O. R. Moheimani, "Kalman filter enabled high-speed control of a MEMS nanopositioner," *IFAC-PapersOnLine*, vol. 50, no. 1, pp. 15554–15560, Jul. 2017.

[33] B. A. Francis and W. M. Wonham, "The internal model principle of control theory," *Automatica*, vol. 12, no. 5, pp. 457–465, Sep. 1976.

[34] M. Maroufi and S. O. R. Moheimani, "A 2DOF SOI-MEMS nanopositioner with tilted flexure bulk piezoresistive displacement sensors," *IEEE Sensors J.*, vol. 16, no. 7, pp. 1908–1917, Apr. 2016.

[35] A. Cowen, G. Hames, D. Monk, S. Wilcenski, and B. Hardy, *SOI-MUMPs Design Handbook, Revision 8.0*. Durham, NC, USA: MEMSCAP Inc., 2011.

[36] M. Maroufi, A. Bazaei, A. Mohammadi, and S. O. R. Moheimani, "Tilted beam piezoresistive displacement sensor: Design, modeling, and characterization," *J. Microelectromech. Syst.*, vol. 24, no. 5, pp. 1594–1605, Oct, 2015.

[37] A. Bazaei, M. Maroufi, and S. O. R. Moheimani, "Tracking of constant-linear-velocity spiral trajectories by approximate internal model control," in *Proc. IEEE Conf. Control Technol. Appl. (CCTA)*, Aug. 2017, pp. 129–134.

[38] A. Lanzon and I. R. Petersen, "Stability robustness of a feedback interconnection of systems with negative imaginary frequency response," *IEEE Trans. Autom. Control*, vol. 53, no. 4, pp. 1042–1046, May 2008.

[39] Y. R. Teo, Y. K. Yong, and A. J. Fleming, "A review of scanning methods and control implications for scanning probe microscopy," in *Proc. Amer. Control Conf. (ACC)*, Jul. 2016, pp. 7377–7383.

[40] A. J. Fleming and A. G. Wills, "Optimal periodic trajectories for band-limited systems," *IEEE Trans. Control Syst. Technol.*, vol. 17, no. 3, pp. 552–562, May 2009.

[41] M. Maroufi, H. Alemansour, M. B. Coskun, and S. O. R. Moheimani, "An adjustable-stiffness MEMS force sensor: Design, characterization, and control," *Mechatronics*, to be published, doi: 10.1016/j.mechatronics.2018.05.007.

[42] J. G. Proakis and D. K. Manolakis, *Digital Signal Processing*. 4th ed. Upper Saddle River, NJ, USA: Prentice-Hall, 2006.

Nastaran Nikooienejad received the B.Sc. degree in Electrical Engineering from Shiraz University, Shiraz, Iran, in 2006, and the M.Sc. degree in Electrical Engineering from Amirkabir University of Technology, Tehran, Iran, in 2009. She is currently pursuing the Ph.D. degree with the Department of Electrical Engineering, The University of Texas at Dallas, Richardson, TX, USA.

Her current research interests include control of MEMS nanopositioners, non-raster scanning methods, video-rate atomic force microscopy, signal and image processing.

Afshin Alipour received the B.Sc. degree in Mechanical Engineering from Amirkabir University of Technology, Tehran, Iran, in 2013, and the M.Sc. degree in Applied Mechanics from the University of Tehran, Tehran, in 2016. He is currently pursuing the Ph.D. degree with the Department of Mechanical Engineering, The University of Texas at Dallas, Richardson, TX, USA.

His current research interests include the fields of dynamics, vibrations, and control.

Mohammad Maroufi received double B.Sc. degree in Mechanical Engineering and Applied Physics and M.Sc. degree in Mechatronics from Amirkabir University of Technology (Tehran Polytechnic) in 2008 and 2011, respectively. In 2015, he obtained his Ph.D. in Electrical Engineering at the University of Newcastle, Callaghan, NSW, Australia.

Dr. Maroufi is currently a Research Scientist with the Department of System Engineering, The University of Texas at Dallas, Richardson, TX, USA. His research interests include development of high-precision mechatronic systems, design and control of MEMS nanopositioners, microsensors design, and video-rate Atomic Force Microscopy.

S. O. Reza Moheimani currently holds the James Von Ehr Distinguished Chair in science and technology with the Department of System Engineering, The University of Texas at Dallas, Richardson, TX, USA. He is also an Adjunct Professor with the University of Newcastle, Callaghan, NSW, Australia. His current research interests include ultrahigh-precision mechatronic systems with particular emphasis on dynamics and control at the nanometer scale, including applications of control and estimation in nanopositioning systems for high-speed scanning probe microscopy and nanomanufacturing, modeling and control of microcantilever-based devices, control of microactuators in microelectromechanical systems, and design, modeling, and control of micromachined nanopositioners for on-chip scanning probe microscopy.

Dr. Moheimani is a Fellow of IFAC and the Institute of Physics, U.K. He is the Editor-in-Chief of Mechatronics and has served on the editorial boards of a number of other journals, including the IEEE TRANSACTIONS ON MECHATRONICS, the IEEE TRANSACTIONS ON CONTROL SYSTEMS TECHNOLOGY, and *Control Engineering Practice*. He was the Chair of the IFAC Technical Committee on Mechatronic Systems from 2011 to 2017. He was a recipient of several awards, including IFAC Nathaniel B. Nichols Medal in 2014, the IFAC Mechatronic Systems Award in 2013, the IEEE Control Systems Technology Award in 2009, the IEEE TRANSACTIONS ON CONTROL SYSTEMS TECHNOLOGY Outstanding Paper Award in 2007, and several best paper awards in various conferences.